ADVANCED ENERGY MATERIALS
www.advenergymat.de

Operando Lithium Dynamics in the Li-Rich Layered Oxide Cathode Material via Neutron Diffraction

*Haodong Liu, Yan Chen, Sunny Hy, Ke An, Subramanian Venkatachalam, Danna Qian, Minghao Zhang, and Ying Shirley Meng**

Neutron diffraction under operando battery cycling is used to study the lithium and oxygen dynamics of high Li-rich $Li(Li_{x/3}Ni_{(3/8-3x/8)}Co_{(1/4-x/4)}Mn_{(3/8+7x/24)}O_2$ (x = 0.6, HLR) and low Li-rich $Li(Li_{x/3}Ni_{(1/3-x/3)}Co_{(1/3-x/3)}Mn_{(1/3+x/3)}O_2$ (x = 0.24, LLR) compounds that exhibit different degrees of oxygen activation at high voltage. The measured lattice parameter changes and oxygen position show largely contrasting changes for the two cathodes where the LLR exhibits larger movement of oxygen and lattice contractions in comparison to the HLR that maintains relatively constant lattice parameters and oxygen position during the high voltage plateau until the end of charge. Density functional theory calculations show the presence of oxygen vacancy during the high voltage plateau; changes in the lattice parameters and oxygen position are consistent with experimental observations. Lithium migration kinetics for the Li-rich material is observed under operando conditions for the first time to reveal the rate of lithium extraction from the lithium layer, and transition metal layer is related to the different charge and discharge characteristics. At the beginning of charging, the lithium extraction predominately occurs within the lithium layer. Once the high voltage plateau is reached, the lithium extraction from the lithium layer slows down and extraction from the transition metal layer evolves at a faster rate.

1. Introduction

The progressive advancements in communication and transportation have changed human daily life to a great extent.[1] With the birth of the secondary lithium ion battery, the past few decades have moved mobile devices and personal computer devices from novelty to an almost essential necessity in order to function in a modern day society. While important advancements in battery technology have come since its first demonstration, the high energy demands needed to electrify the automotive industry have not yet been met with the current technology.[2,3] One considerable bottleneck is the cathode energy density.[2,3] The lithium layered oxides utilize transition metal redox pairs for charge/discharge compensation during lithium extraction and intercalation offering a theoretical capacity of 270 mAh g^{-1} for complete lithium extraction.[3,4] However, practical capacities have so far shown to be ≈200 mAh g^{-1} due to degradation reactions and large lattice contractions at low lithium content, limiting its capability to meet future demands. One possible cathode material is the Li-rich layered oxide compounds $x Li_2MnO_3 \cdot (1-x) LiMO_2$ (M = Ni, Mn, Co) ($0.5 = < x = < 1.0$) that exhibit capacities over 280 mAh g^{-1} obtainable by the combination of the typical transition metal redox pair with the additional oxygen redox reaction as the charge compensation mechanism.[5] In this class of compounds, lithium ions can reside in both lithium layer and transition metal layer of close packed oxygen framework, typical from O3 type layered oxides like $LiCoO_2$. Large irreversible capacities are often observed in these materials due to irreversible oxygen loss or side reactions stemming for the electrolyte.[6] It has been also observed using ex situ NMR (nuclear magnetic resonance) that lithium reinsertion back into the transition metal layer is little to none.[7] Several different lithium extraction/insertion sites and migration pathways are available, where lithium may be extracted from lithium or transition metal layers and lithium from octahedral coordinated sites to tetrahedral sites to form Li–Li dumbbells.[8] However, these studies have not revealed the dynamic process of lithium migration for the Li-rich material under operando electrochemical cycling conditions.

Neutron scattering has several distinct advantages for battery studies: (1) The sensitivity of neutron to light elements such as lithium and oxygen is significant in order to determine their position in the crystal structure; (2) Compares to the X-ray, the neutron shows larger scattering contrast between neighboring elements in the periodic table specifically the scattering lengths, e.g., for transition metals in this case: Ni, 10.3 fm; Mn, −3.73 fm; Co, 2.49 fm; and (3) The deep penetration capability of neutron allows simultaneous observation of the cathode and

H. Liu, Dr. S. Hy, Dr. D. Qian, M. Zhang, Prof. Y. S. Meng
Department of NanoEngineering
University of California
San Diego, La Jolla, CA 92093, USA
E-mail: shirleymeng@ucsd.edu
Dr. Y. Chen, Dr. K. An
Chemical and Engineering Materials Division
Oak Ridge National Laboratory
Oak Ridge, TN 37830, USA
Dr. S. Venkatachalam
Envia Systems
7979 Gateway Building
Suite 101, Newark, CA 94560, USA

DOI: 10.1002/aenm.201502143

 © 2016 WILEY-VCH Verlag GmbH & Co. KGaA, Weinheim

anode. However, challenges exist in broadening the application of operando neutron diffraction for Li-ion batteries research. First, limited by the generation reactions of neutrons, the neutron flux is usually several orders of magnitude lower than X-rays. In another words, longer acquisition times as well as larger amounts of samples are required for neutron diffraction experiments. In addition, the existence of hydrogen, which has a large incoherent neutron-scattering cross-section, is detrimental to the signal-to-noise ratio of neutron diffraction pattern. Separators (polyethylene based porous membrane) and poly carbonate based electrolyte solutions contain a considerable amount of hydrogen. These two major reasons pose significant challenges to operando neutron diffraction for lithium ion battery research although it is such a powerful technique for light elements like lithium.[9] Several groups designed special strategies to overcome these problems. Novak and co-workers designed large electrochemical cells with special configuration to guarantee enough active material exposure to the incident neutron beam.[10] Sharma and co-workers used expensive deuterated electrolytes to minimize the noise from hydrogen.[11] Vadlamani et al. selected single crystal (100) Si sheets as casing material, which improved signal-to-noise ratio relative to other casing materials.[12]

In order to gain more in-depth insights about the lithium (de-)intercalation mechanisms in Li-rich layered oxides, track particularly the lithium ions in transition metal layer, operando neutron diffraction experiments were designed to quantitatively observe lithium migration in this type of oxides during the electrochemical process. Here, we use amorphous silicon as an anode for the neutron diffraction battery design in order to avoid any overlap of signal that may be associated with the anode material. We perform operando neutron diffraction to probe lithium and oxygen for a high Li-rich (HLR), $Li(Li_{x/3}Ni_{(3/8-3x/8)}Co_{(1/4-x/4)}Mn_{(3/8+7x/24)}O_2$ (x = 0.6) material, and low Li-rich (LLR), $Li(Li_{x/3}Ni_{(1/3-x/3)}Co_{(1/3-x/3)}Mn_{(1/3+x/3)}O_2$ (x = 0.24) material with varying degrees of the high voltage plateau. In conjunction with the operando neutron diffraction, density functional theory (DFT) calculations were used to explore the incorporation of dilute oxygen vacancy, its effect on the lattice mechanics and oxygen positions. We also observe site-dependent lithium migration taking place during different stage of charging/discharge processes. To our knowledge, this is the first time differentiation of lithium migration has been observed and identified during battery operation for this class of materials. Furthermore, this work demonstrates the potential of investigating dynamic changes of light elements in large format (10–100 times larger format than the typical operando cells for synchrotron X-ray diffraction) prismatic and cylindrical batteries under realistic cycling condition via operando neutron diffraction method.

2 Results and Discussions

2.1. Neutron Diffraction Battery Device and Electrode Materials

Figure 1a shows the operando neutron diffraction experiment set up. The incident neutrons are continuously scattered by the pouch cell during constant current charge/discharge. The scattered neutrons are recorded by the detectors in real time. A thick pouch cell with 12 layers was designed to increase the amount of cathode material in the scattering volume, which achieves better signal than the previous single layer cell.[9] Figure S1 (Supporting Information) shows operando neutron diffraction plots of LR/graphite cell and for the HLR/Si cell during charge (5 h charging data). For the graphite cell, the

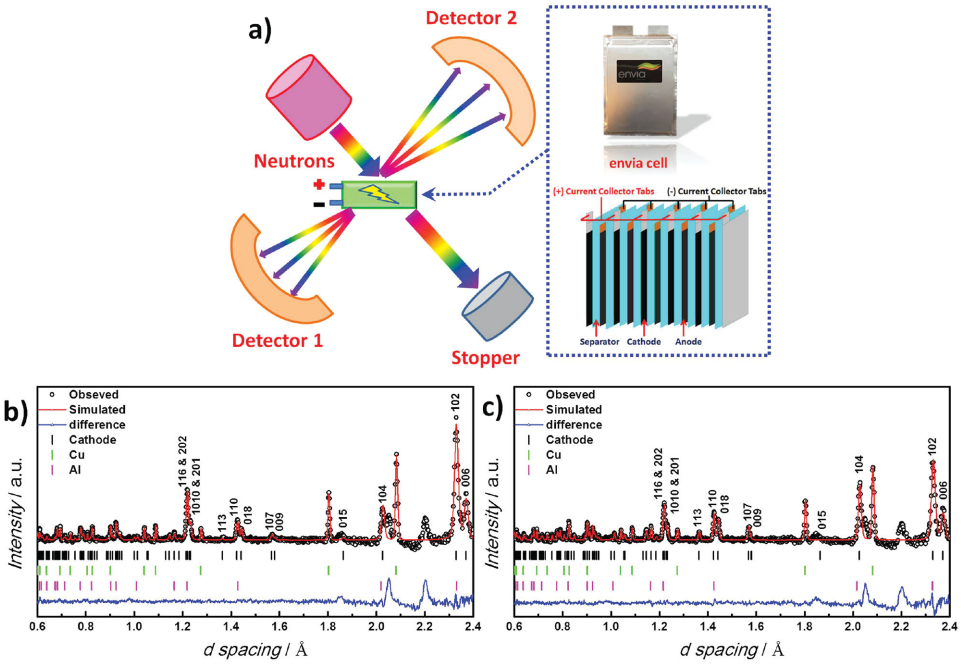

Figure 1. a) Schematic of the operando neutron diffraction study and the pouch cell. b) Refined diffraction pattern of HLR/Si cell and c) LLR/Si cell at the open circuit potential state.

© 2016 WILEY-VCH Verlag GmbH & Co. KGaA, Weinheim

Table 1. Refinement results of the HLR (top) and LLR (bottom) batteries at the open circuit voltage (OCV) state.

	a_{hex} [Å]	c_{hex} [Å]	Li/Ni mixing	Oxygen coordinates	R_{wp} [%]	χ^2
HLR	2.8465(2)	14.217(2)	0.045(7)	0.2412(2)	1.20	1.70
LLR	2.8481(2)	14.227(2)	0.026(6)	0.2406(2)	1.06	1.40

evolution of peaks from the cathode and anode shows several overlapping Bragg peaks of graphite and LR. The refinement and challenges of LR/graphite cell are detailedly described in the Supporting Information. We redesigned the multilayered pouch cell by replacing the graphite anode with an amorphous silicon anode. For the HLR/Si cell, the evolution of (110), (108), (107), (104), (102), and (006) peaks from cathode can be clearly distinguished when compared to the LR/graphite cell.

Figure 1b,c shows the refined patterns of the HLR and LLR/Si cell before any electrochemical cycling where no signal from anode is observed and the weight profile factor R_{wp} is reduced. **Table 1** compares the refinement results of the HLR and LLR cathode batteries before cycling. For the purpose of comparison, the R$\bar{3}$m layered structure was used for the refinement of the HLR and LLR. The Li/Ni mixing was found to be 4.5(7)% in HLR, which is slightly higher than LLR that showed 2.6(6)%.

2.2. Lattice Dynamics and Lattice Oxygen Evolution during Battery Charge and Discharge

Figure 2a,b shows the charge/discharge voltage profile of HLR and LLR/Si cell, respectively, which was charged to 4.7 V at constant current of 80 mA, then discharged to 1.5 V at 80 and 120 mA (discharge at higher current due to the limited beam-time), respectively. The HLR/Si full cell shows a typical voltage profile of the Li-rich material that includes three distinct regions described as followed: (1) a slope region <4.3 V that is predominately the Ni $^{2+/4+}$ redox pair, (2) a plateau region >4.3 V that involves the simultaneous extraction of oxygen and lithium where oxygen participates in the charge compensation mechanism, and (3) a single slope during the first discharge that is a combination of transition metal redox pairs and oxygen participation.[13,14] Based on the capacity, there are 0.865 Li^+ extracted out from HLR cathode at the end of charge, and 0.562 Li^+ inserted back after discharge. Due to the low efficiency of Si anode, the first cycle coulombic efficiency of this full cell is 64.4%. The LLR/Si full cell shows a longer slope region due to high nickel content and shorter plateau region compared to the HLR/Si full cell. There are 0.942 Li^+ extracted out from LLR cathode at the end of charge, and 0.617 Li^+ inserted back after discharge, leading to a 65.4% first cycle coulombic efficiency that is comparable to the HLR/Si cell.

The lattice parameters of both cells are plotted in Figure 2a,b, respectively. Before charge, the *a* and *c* lattice parameters of HLR are 2.8465(2) Å and 14.217(2) Å, respectively. During the slope region, Li^+ is extracted from the layered structure while Ni^{2+} and Co^{3+} are oxidized to Ni^{4+} and Co^{4+}, and that causes the ionic radii to decrease (e.g., r Ni^{2+} = 0.69 Å, r Ni^{3+} = 0.60 Å, r Ni^{4+} = 0.48 Å), leading to a rapid contraction of the *a* lattice parameter to 2.8265(3) Å (0.70% smaller than open circuit voltage (OCV) state).[9] The refined oxygen positions were plotted in **Figure 3**a in red circles. The oxidation of TM ions increased the electrostatic attraction between the TM ions and oxygen ions that decreases the bond length of TM—O. On the other hand, the removal of Li^+ introduces a concentration gradient and electrostatic repulsion from adjacent oxygen layers accounting for the increasing of *c* lattice parameter to 14.381(4) Å (1.15% larger than OCV state). As a comparison, the *a* lattice parameter of LLR decreased 1.16% from 2.8481(2) Å to 2.8150(3) Å, and the *c* lattice parameter of LLR increased 1.65% from 14.227(2) Å to 14.462(3) Å. The larger changes of lattice parameters of LLR after the slope region are caused by the higher concentration of TM ions having been oxidized.

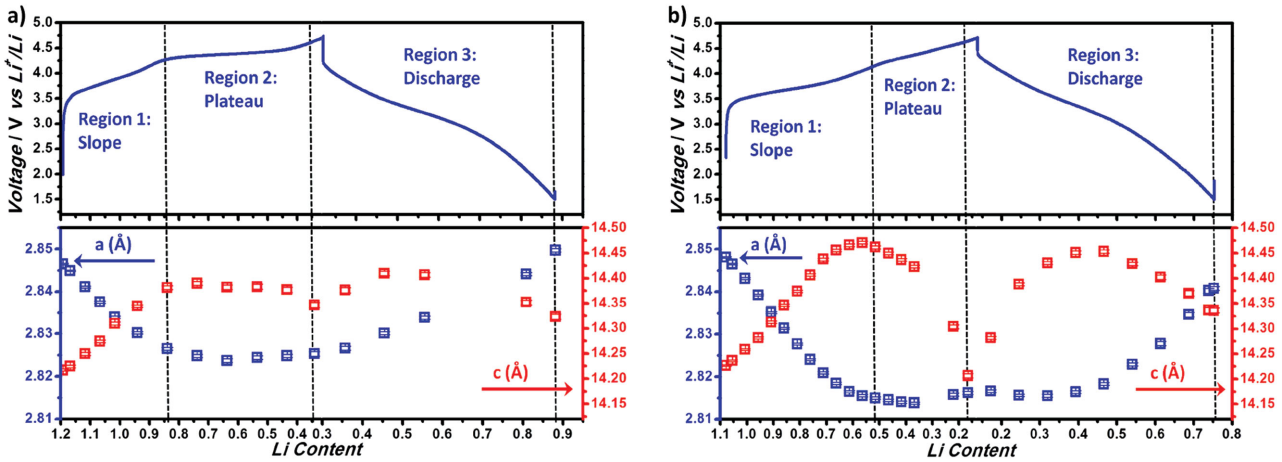

Figure 2. Electrochemical charge/discharge profile with corresponding lattice parameters at different states of delithiation/lithiation for a) HLR and b) LLR.

© 2016 WILEY-VCH Verlag GmbH & Co. KGaA, Weinheim

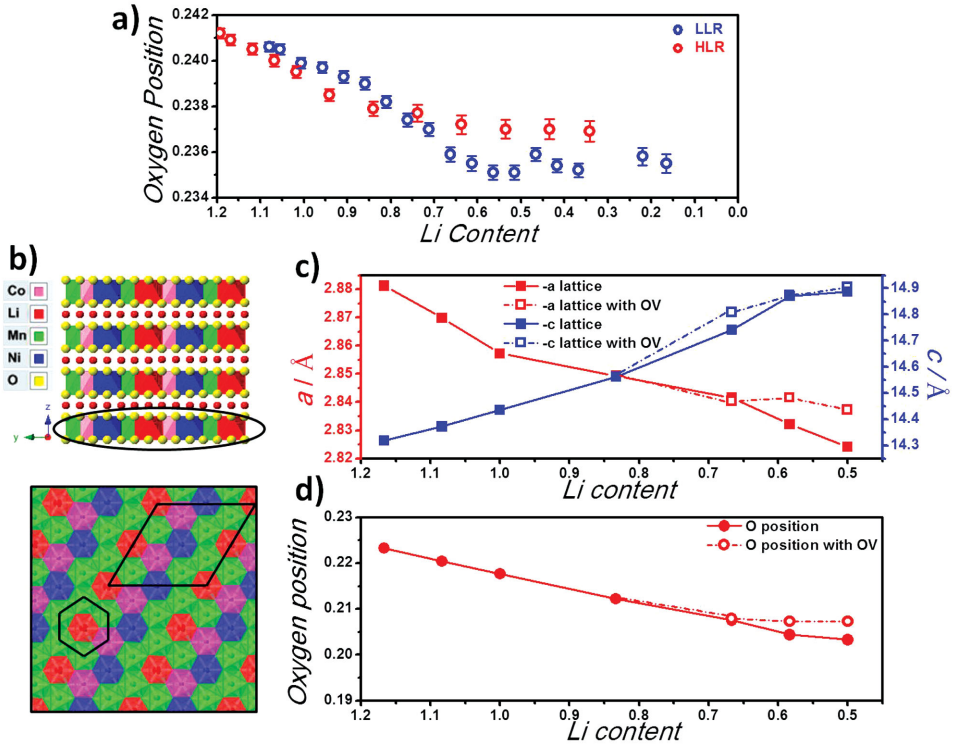

Figure 3. a) Oxygen position from refinement results, b) the cation ordering in TM layer used for DFT calculations, c) DFT results of the evolution of the lattice parameters, and d) oxygen position with and without oxygen vacancy.

All the TM ions stay in their highest oxidation state without further oxidation during the plateau region, which causes the *a* lattice parameter remaining relatively constant. The oxygen position is also observed to be constant in this plateau region indicating the TM ions do not participate in the charge compensation process during this plateau region. With the Li^+ continuously being extracted, out of expectations, the *c* lattice parameter of HLR decreased slightly to 14.346(5) Å (0.24% smaller than end of slope) at the charged state. However, the *c* lattice parameter of LLR dramatically decreased to 14.206(4) Å (1.77% smaller than end of slope) at the charged state even beyond the pristine state. The contraction of *c* lattice parameter is less severe or delayed in HLR compared to the LLR as a result of the higher degree of oxygen activity as indicated by the longer high voltage plateau, which is consistent with previous in situ X-ray studies.[13,15,16]

The first-principles calculations were performed to gain more insight to the changes in lattice parameters[17] and oxygen positions. The supercell is composed of 12-formula units of $Li(Li_{1/6}Ni_{1/6}Co_{1/6}Mn_{1/2})O_2$. For the convenience to interpret the delithiation in computation, the formula of this compound will be written in the form of $Li_{14/12}Ni_{2/12}Co_{2/12}Mn_{6/12}O_2$. As shown in Figure 3, oxygen ions are close-packed and stacked in ABCABC (O3) stacking, while TM layers and lithium layers stack alternatively in the octahedron sites. The cation ordering in TM layer is plotted in Figure 3, each Li^+ is surrounded by 5 Mn^{4+} and 1 Co^{3+}. The lattice parameters and oxygen positions are calculated as a function of lithium content in the structure. The range of $Li_{14/12}$ to $Li_{8/12}$ corresponds to the slope region, and $Li_{8/12}$ to $Li_{6/12}$ corresponds to the plateau region. The computational results show a decrease of *a* lattice parameter and oxygen position, while the *c* lattice parameter expands during the slope region. Thus, the trend of the lattice parameters and oxygen position is consistent with the experimental results in this region. However, the computational results show discrepancy from experimental results where a continuous change occurs in the lattice parameters and oxygen position at the plateau region. We created a dilute oxygen vacancy (1/24) model and simulated the delithiation from $Li_{8/12}Ni_{2/12}Co_{2/12}Mn_{6/12}\square_{1/12}O_{23/12}$ to $Li_{6/12}Ni_{2/12}Co_{2/12}Mn_{6/12}\square_{1/12}O_{23/12}$. The computational results for the oxygen vacancy model are in good agreement with the experimental results showing constant lattice parameters and little oxygen movement during the high voltage plateau region.

As Li^+ is inserted back to HLR cathode during discharge, the *a* lattice parameter increased monotonically to 2.8497(4) Å, which is 0.11% larger than the pristine state. The increase of the *a* lattice parameter and elongation of TM—O bond are caused by the reduction of TM ions during discharge. The changes of *c* lattice parameter during discharge are complex, which increased at first then decreased to 14.323(5) Å (0.75% larger than OCV state). The trends in the lattice parameters as function of the state of charge for HLR are quite consistent with previous in situ XRD studies.[16] Similar to the HLR, both *a* and *c* lattice parameters of LLR suffered irreversible changes after the first cycle, the *c* lattice parameter becomes 14.336(5) Å (0.77% larger than OCV state). However, the *a* lattice parameter increased monotonically only to 2.8408(5) Å during discharge, which is 0.26% smaller than the pristine state. These changes in *a* lattice parameter show little discrepancy with previous study. We ascribe this to the low efficiency of Si anode, which limited the amount of lithium inserts

© 2016 WILEY-VCH Verlag GmbH & Co. KGaA, Weinheim

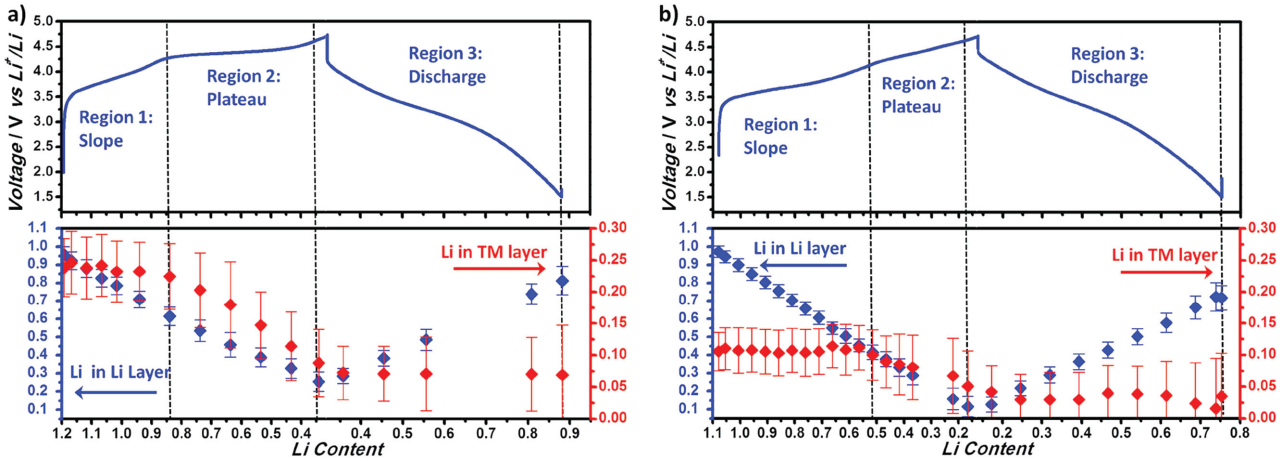

Figure 4. Electrochemical charge/discharge profile with corresponding lithium occupancy at different states of delithiation/lithiation for a) HLR and b) LLR.

back to the LLR. To our best knowledge, this operando neutron study to investigate the lattice dynamics and lattice oxygen evolution in a full cell configuration is reported for the first time.

2.3. Operando Observation of Path-Specific Lithium Migration

Based on the R$\bar{3}$m layered structure, there are two different lithium sites within Li-rich layered oxide. Most of the Li^+ is located within the lithium layer, while the excess amount of Li^+ stay within TM layer as indicated by the refinement results for HLR and LLR before cycling. As shown in **Figure 4**a, during the slope region, the Li^+ in lithium layer is observed to be extracted out with little to no extraction from the TM layer. A similar trend was also observed for LLR in Figure 4b. DFT calculations was carried out to verify the experimental observations by comparing the energies of removing different Li^+. At fully lithiated state, the results from calculations showed that the extraction of Li^+ from TM layer will consume more energy (0.5505 eV per unit cell) than the removal of Li^+ from the lithium layer.

During the first charge plateau region, Li^+ was observed to be extracted from both the lithium layer and TM layer. Based on the reported experimental and computational studies, a certain amount of tetrahedral Li would likely form during this plateau.[8,18] These tetrahedral site lithium will block Li^+ from going back to the TM layer. As a sequence, when Li^+ inserts back to Li-rich layered oxide during discharge, all the Li^+ goes back to the lithium layer. After the first cycle, the lithium content in HLR TM layers irreversibly decreased to 0.069(78) (29% of its OCV state) and 0.035(68) (33% of its OCV state) for LLR. Similar results have been reported by NMR spectroscopy,[7,19] it is found very few Li^+ can be intercalated back into the TM layer after being charged at high voltages.

The Li^+ extraction/insertion rates of both HLR and LLR during different regions in their first charge/discharge were calculated and the detailed results are listed in **Table 2**. At the beginning of charging, the rate of lithium extraction within lithium layers for the slope region is 8.08×10^{-4} atoms min^{-1} and 7.75×10^{-4} atoms min^{-1} for HLR and LLR, respectively. Li^+ extraction rate within the TM layer for this region is relatively slow in comparison with 0.333×10^{-4} atoms min^{-1} and 0.075×10^{-4} atoms min^{-1} for HLR and LLR, respectively. The corresponding rates of change of the *a* and *c* lattice parameters are -4.83×10^{-5} and 3.90×10^{-4} Å min^{-1} for HLR and -4.67×10^{-5} and 3.26×10^{-4} Å min^{-1} for the LLR. Interestingly, in the plateau region for HLR, the rate of Li^+ extraction decreases in the lithium layer to 5.85×10^{-4} atoms min^{-1} and increases in the TM layer to 2.22×10^{-4} atoms min^{-1}. Similarly, for LLR in the plateau region, the extraction rate within the lithium layer also slows down slightly to 6.93×10^{-4} atoms min^{-1} and increases to 1.10×10^{-4} atoms min^{-1} from the TM layer. The corresponding rates of change in the *a* lattice parameter for HLR and LLR are relatively small ($\approx 10^{-6}$ Å min^{-1}) for the plateau region while the *c* lattice parameter rates within the plateau region are -5.67×10^{-5} and -5.92×10^{-4} Å min^{-1} for the HLR and LLR, respectively. The extraction rate of Li^+ in transition metal layer in HLR is two times that of LLR and the decrease in rates for HLR and LLR within the lithium layer are 27.6% and

Table 2. Lithium extraction rate based on different regions during electrochemical charging.

Site	Electrochemical charge region	C-rate [C = 250 mAh g^{-1}]	Extraction/insertion rate atoms [min^{-1}]
Li_{TM}(HLR)	Slope	C/15	0.333×10^{-4}
Li_{Li}(HLR)	Slope	C/15	8.08×10^{-4}
Li_{TM}(HLR)	Plateau	C/15	2.22×10^{-4}
Li_{Li}(HLR)	Plateau	C/15	5.85×10^{-4}
Li_{TM}(HLR)	Discharge	C/15	–
Li_{Li}(HLR)	Discharge	C/15	8.42×10^{-4}
Li_{TM}(LLR)	Slope	C/15	0.075×10^{-4}
Li_{Li}(LLR)	Slope	C/15	7.75×10^{-4}
Li_{TM}(LLR)	Plateau	C/15	1.10×10^{-4}
Li_{Li}(LLR)	Plateau	C/15	6.93×10^{-4}
Li_{TM}(LLR)	Discharge	C/10	–
Li_{Li}(LLR)	Discharge	C/10	1.17×10^{-3}

© 2016 WILEY-VCH Verlag GmbH & Co. KGaA, Weinheim

8%, respectively. As previous computation study has indicated, the existence of oxygen vacancies lowers the diffusion barriers for cations in TM layer.[20] Over the entire charging region, the total Li extraction rate is similar for both HLR and LLR. The differences in the total lithium extraction between the slope and plateau region for the two materials are related to the different charging compensation mechanisms that dominate the respective regions. For LLR, the slope region, where the transition metal redox pair reaction ($Ni^{2+/4+}$ and $Co^{3+/4+}$) occurs, is the dominant mechanism extracting a total of ≈0.57 Li. In comparison, the plateau region for LLR, where oxygen is involved, ≈0.35 Li is extracted. For HLR where oxygen involvement is more dominant, the slope region has a total of ≈0.36 Li while the plateau region has a total of ≈0.49 Li extracted. Considering the relatively higher Ni content in the LLR (0.253) versus the HLR (0.15), the length of the slope region is appropriate. The region specific extraction rate of Li^+ in the TM layer for both the LR materials and the computation results may suggest that the formation of oxygen vacancy can facilitate the migration of lithium from the transition metal layer or possibly migration of lithium to tetrahedral sites. In any case, the migration behavior of the two Li-rich materials shows that the rate of lithium extraction and reinsertion for the slope, plateau, and discharge regions during electrochemical cycling is path-dependent.

3. Conclusion

Operando neutron diffraction on a high Li-rich and low Li-rich cathode was performed during battery operation using a custom 1 Ah pouch battery with amorphous silicon to isolate structural changes for the cathode. Evolution of the lattice parameters and oxygen position revealed large lattice contractions occurring for the low Li-rich cathode and a largely delayed change in the high Li-rich cathode at higher voltages. Lithium dynamics were observed and quantified. It is revealed for the first time that lithium migration rates at different sites are highly dependent on the different voltage regions that exhibit different battery characteristics. First, the extraction of lithium at the slope region is largely dominated by migration within lithium layers. During the plateau region, lithium migration within lithium layers slows down and migration from the transition metal layer occurs. Upon discharge, lithium from the transition metal layer is largely irreversible with only lithium reinsertion occurring within lithium layers. These results provide new insights into the lithium migration behavior in lithium rich layered oxides and demonstrate the unique capabilities to observe light elements in the bulk under operando conditions via neutron diffraction.

4. Experimental Section

Material: HLR and LLR cathode materials were generously provided by Envia Systems. The materials were synthesized via a co-precipitation route and details are provided elsewhere.[21] Inductively coupled plasma atomic emission spectroscopy (ICP-AES) was used to determine the composition of lithium and transition metal of the HLR and LLR cathode materials. Those data were then used as initial parameters for the Rietveld refinement of the neutron diffraction patterns.

Cell Design: The cells were designed and assembled in a dry room at Envia's fabrication facility. The cell included 12 pieces of dual sided anode (graphite or amorphous silicon) and Li-rich layered cathode. This cell configuration and design aimed at increasing the loading of active materials in our pouch cells to increase neutron diffraction pattern statistics. A Celgard separator was used to alternatively cover the anode and cathode on each side. The electrolyte solution composed of 1 M $LiPF_6$ in a 1:1 ethylene carbonate (EC):diethyl carbonate. The cathode was composed of 92% active material, 4% polyvinylidene fluoride (PVDF), and 4% carbon black on an aluminum current collector.

Operando Neutron Diffraction: A Bio-Logic SP-300 potentiostat was used to electrochemically cycle the cell under constant charge and discharge currents. The $Li(Li_{x/3}Ni_{(3/8-3x/8)}Co_{(1/4-x/4)}Mn_{(3/8+7x/24)}O_2$ ($x = 0.6$, HLR)/Si pouch cell was charged at 80 mA (≈ C/15) to 4.7 V then discharged at –80 mA to 1.5 V. The $Li(Li_{x/3}Ni_{(1/3-x/3)}Co_{(1/3-x/3)}Mn_{(1/3+x/3)}O_2$ ($x = 0.24$, LLR)/Si pouch cell was charged at 80 mA (≈C/15) to 4.7 V then discharged at –120 mA to 1.5 V (≈C/10). The time of fight powder neutron diffraction data were collected on the VULCAN beamline at the Spallation Neutron Sources (SNS) in the Oak Ridge National Laboratory.[22] An incident beam (5 mm × 12 mm) of 0.7 to 3.5 Å bandwidth allowing 0.5≈2.5 Å d-space in diffracted patterns in the ±90° 2θ detector banks was selected using the double-disk choppers at 30 Hz speed. High intensity mode was employed with $\Delta d/d \approx 0.45\%$. The SNS power was at nominal 1100 KW.[22] Time stamped neutron event data were collected while the cells were under continuous cycling. Neutron diffraction data were sliced and reduced by the VDRIVE software.[23] Full pattern Rietveld refinement was performed using the GSAS programs with the EXPGUI interface.[24]

The operando neutron diffraction data were sliced every 3600 or 7200 s and reduced by the VDRIVE software.[23] Multiphase Rietveld refinement was carried out to analyze the structure evolution of Li-rich cathode as a function of state of charge. The multiphase refinement model includes Li-rich cathode,[9,25] cathode current collector Al, and anode current collector Cu. The texture and crystal structure of Al and Cu were optimized for the first data set and subsequently fixed in the following data. In each data set, the lattice parameters, lithium occupancies, and oxygen positions were refined. The weight profile factor R_{wp} is usually < 1.31%.

Computation Methods: The first-principles calculations were performed in the spin polarized generalized gradient approximations (GGA) to the DFT. Core electron states were represented by the projector augmented-wave method[26] as implemented in the Vienna ab initio simulation package.[27] The Perdew–Burke–Ernzerhof exchange correlation[28] and a plane wave representation for the wavefunction with a cutoff energy of 450 eV were used. The Brillouin zone was sampled with a dense kpoints mesh by Gamma packing.

Supporting Information

Supporting Information is available from the Wiley Online Library or from the author.

Acknowledgements

UCSD's efforts were supported by the Assistant Secretary for Energy Efficiency and Renewable Energy, Office of Vehicle Technologies of the U.S. Department of Energy (DOE) under Contract No. DE-AC02-05CH11231, Subcontract No. 7073923, under the Advanced Battery Materials Research (BMR) Program. The neutron experiments benefited from the SNS user facility, sponsored by the office of Basic Energy Sciences (BES), the Office of Science of the DOE. H.L. acknowledges the financial support from the China Scholarship Council under Award No. 2011631005. Y.C. acknowledges the support from U.S. DOE's Office of Basic Energy Sciences, Material Science and Engineering Division. This work used the Extreme Science and Engineering Discovery Environment

© 2016 WILEY-VCH Verlag GmbH & Co. KGaA, Weinheim

(XSEDE), which was supported by National Science Foundation grant number ACI-1053575.

Received: October 29, 2015
Revised: December 15, 2015
Published online:

[1] J. B. Goodenough, K.-S. Park, *J. Am. Chem. Soc.* **2013**, *135*, 1167.
[2] D. Andre, S.-J. Kim, P. Lamp, S. F. Lux, F. Maglia, O. Paschos, B. Stiaszny, *J. Mater. Chem. A* **2015**, *3*, 6709.
[3] M. S. Whittingham, *Chem. Rev.* **2004**, *104*, 4271.
[4] J. J. Huang, J. Luo, *Phys. Chem. Chem. Phys.* **2014**, *16*, 7786.
[5] a) H. Koga, L. Croguennec, M. Ménétrier, K. Douhil, S. Belin, L. Bourgeois, E. Suard, F. Weill, C. Delmas, *J. Electrochem. Soc.* **2013**, *160*, A786; b) H. Koga, L. Croguennec, M. Ménétrier, P. Mannessiez, F. Weill, C. Delmas, *J. Power Sources* **2013**, *236*, 250; c) M. Sathiya, G. Rousse, K. Ramesha, C. P. Laisa, H. Vezin, M. T. Sougrati, M. L. Doublet, D. Foix, D. Gonbeau, W. Walker, A. S. Prakash, M. Ben Hassine, L. Dupont, J. M. Tarascon, *Nat. Mater.* **2013**, *12*, 827.
[6] M. G. Verde, H. D. Liu, K. J. Carroll, L. Baggetto, G. M. Veith, Y. S. Meng, *ACS Appl. Mater. Inter.* **2014**, *6*, 18868.
[7] F. Dogan, B. R. Long, J. R. Croy, K. G. Gallagher, H. Iddir, J. T. Russell, M. Balasubramanian, B. Key, *J. Am. Chem. Soc.* **2015**, *137*, 2328.
[8] B. Xu, C. R. Fell, M. Chi, Y. S. Meng, *Energ. Environ. Sci.* **2011**, *4*, 2223.
[9] H. D. Liu, C. R. Fell, K. An, L. Cai, Y. S. Meng, *J. Power Sources* **2013**, *240*, 772.
[10] a) F. Rosciano, M. Holzapfel, W. Scheifele, P. Novak, *J. Appl. Crystallogr.* **2008**, *41*, 690; b) J. J. Biendicho, M. Roberts, C. Offer, D. Noreus, E. Widenkvist, R. I. Smith, G. Svensson, K. Edstrom, S. T. Norberg, S. G. Eriksson, S. Hull, *J. Power Sources* **2014**, *248*, 900.
[11] W. K. Pang, V. K. Peterson, N. Sharma, J. J. Shiu, S. H. Wu, *Chem. Mater.* **2014**, *26*, 2318.
[12] B. Vadlamani, K. An, M. Jagannathan, K. S. R. Chandran, *J. Electrochem. Soc.* **2014**, *161*, A1731.
[13] Z. H. Lu, J. R. Dahn, *J. Electrochem. Soc.* **2002**, *149*, A815.
[14] a) S. Hy, F. Felix, J. Rick, W. N. Su, B. J. Hwang, *J. Am. Chem. Soc.* **2014**, *136*, 999; b) H. D. Liu, J. Xu, C. Z. Ma, Y. S. Meng, *Chem. Commun.* **2015**, *51*, 4693; c) H. Liu, D. Qian, M. G. Verde, M. Zhang, L. Baggetto, K. An, Y. Chen, K. J. Carroll, D. Lau, M. Chi, G. M. Veith, Y. S. Meng, *ACS Appl. Mater. Inter.* **2015**, *7*, 19189.
[15] A. R. Armstrong, M. Holzapfel, P. Novak, C. S. Johnson, S. H. Kang, M. M. Thackeray, P. G. Bruce, *J. Am. Chem. Soc.* **2006**, *128*, 8694.
[16] L. Simonin, J. F. Colin, V. Ranieri, E. Canevet, J. F. Martin, C. Bourbon, C. Baehtz, P. Strobel, L. Daniel, S. Patoux, *J. Mater. Chem.* **2012**, *22*, 11316.
[17] R. I. Eglitis, *Phys. Scr.* **2015**, *90*, 094012.
[18] D. Mohanty, J. L. Li, D. P. Abraham, A. Huq, E. A. Payzant, D. L. Wood, C. Daniel, *Chem. Mater.* **2014**, *26*, 6272.
[19] M. Jiang, B. Key, Y. S. Meng, C. P. Grey, *Chem. Mater.* **2009**, *21*, 2733.
[20] D. N. Qian, B. Xu, M. F. Chi, Y. S. Meng, *Phys. Chem. Chem. Phys.* **2014**, *16*, 14665.
[21] a) H. A. Lopez, S. Venkatachalam, D. K. K. Karthikeyan, S. Kumar, *US 8741485 B2*, **2014**; b) H. A. Lopez, S. Venkatachalam, D. K. K. Karthikeyan, S. Kumar, *US 8394534 B2*, **2013**; c) S. Venkatachalam, H. Lopez, S. Kumar, *US 8389160 B2*, **2013**.
[22] K. An, H. D. Skorpenske, A. D. Stoica, D. Ma, X. L. Wang, E. Cakmak, *Metall. Mater. Trans. A* **2011**, *42A*, 95.
[23] K. An, X. L. Wang, A. D. Stoica, *ORNL Report* **2012**, 621.
[24] a) A. C. Larson, R. B. V. Dreele, *Los Alamos National Laboratory Report (LAUR)* **2004**, 86; b) B. H. Toby, *J. Appl. Crystallogr.* **2001**, *34*, 210.
[25] J. Xu, H. Liu, Y. S. Meng, *Electrochem. Commun.* **2015**, *60*, 13.
[26] G. Kresse, D. Joubert, *Phys. Rev. B* **1999**, *59*, 1758.
[27] a) G. Kresse, J. Hafner, *Phys. Rev. B* **1994**, *49*, 14251; b) G. Kresse, J. Furthmuller, *Phys. Rev. B* **1996**, *54*, 11169.
[28] J. P. Perdew, K. Burke, Y. Wang, *Phys. Rev. B* **1996**, *54*, 16533.

© 2016 WILEY-VCH Verlag GmbH & Co. KGaA, Weinheim